J. Fluid Mech. (1992), *vol.* 239, *pp.* 607–629
Printed in Great Britain

The evolution of stable barotropic vortices in a rotating free-surface fluid

By R. C. KLOOSTERZIEL[1] AND G. J. F. VAN HEIJST[2]
[1] Institute for Nonlinear Science, University California San Diego, La Jolla, CA 92093, USA
[2] Department of Technical Physics, Eindhoven University of Technology, P.O. Box 513, 5600 MB Eindhoven, The Netherlands

(Received 18 June 1990 and in revised form 10 December 1991)

Laboratory experiments reveal that, for increasing time, barotropic cyclones typically show an increasing steepness in their flow profiles. This implies that such vortices become barotropically more unstable. This has been confirmed by observations which are further discussed in a companion paper (Kloosterziel & van Heijst 1991). In the present paper the evolutionary process is discussed. It is shown that the observed steepening of the flow profiles is mainly a nonlinear effect due to the advection of relative vorticity by the interior Ekman circulation. The linear Ekman pumping law is found to be a good approximation in the core of the vortices for $O(1)$ Rossby numbers but at larger radii the Ekman pumping is stronger in reality. Free-surface effects are shown to have a broadening effect, which can balance the nonlinear steepening if the Rossby number becomes sufficiently small or the Froude number sufficiently large. In addition it is shown that for the classical spin-down problem with a free surface no expansion in the Froude number needs to be introduced.

1. Introduction

In this paper we address the evolution of stable (i.e. topologically invariant with time) axisymmetric vortices, generated by various techniques at the centre of a rotating tank. Free-surface effects (see Carnevale, Kloosterziel & van Heijst 1991) tend to constrain them to such a location. It has furthermore been observed that if initially the vortices deviate slightly from circular symmetry, in the parameter regime studied here they rapidly tend to a circular form. The instability of laboratory vortices is discussed in a companion paper (Kloosterziel & van Heijst 1991).

An overview of the contents of the paper is the following. In §2 the laboratory observations are discussed. After a short description of the laboratory set-up in §2.1, in §2.2 two examples of evolving flow profiles of stable cyclones are presented. The velocity profiles of a so-called 'collapse vortex' and a 'sink vortex' show a distinct 'steepening' as time progresses. Beyond a certain critical steepness such vortices become unstable to wavenumber-2 perturbations which is in accordance with the results of, for instance, Carton & McWilliams (1989). Further details concerning the amplitude decay of a vortex and the shift of the position of its maximum velocity are also presented in §2.2. These data show that the decay rate is faster than linear Ekman decay whereas the shift of the peak velocity is much faster than diffusive spreading.

In §3 we analyse the causes for the observed evolution characteristics. The observed timescale of decay indicates that the evolution of the laboratory vortices is dominated by the Ekman circulation. The evolution problem is therefore attacked by means of an expansion in the (small) Ekman number E. A further systematic scaling analysis shows that there are three other non-dimensional parameters that determine the way a flow profile evolves: the Rossby number, the rotational Froude number and a parameter that compares the diffusive timescale to the Ekman decay time. However, the latter two parameters are very small in the laboratory experiments. It is shown in §3.2 that nonlinear effects, i.e. advection of relative vorticity, induce the observed steepening of the laboratory profiles. Without advection of relative vorticity the well-known linear Ekman dynamics merely leads to an exponential, uniform decay of the vortex. Free-surface effects, that is, effects represented by a non-zero Froude number, are shown to have a broadening effect (see §3.1), but under typical laboratory circumstances this effect is negligibly small.

A key element to the analysis of §3 is the relation between the vertical Ekman pumping at the bottom and the local interior vorticity. For this we tentatively took the well-known Ekman pumping law that follows from the quasi-stationary, linear boundary-layer equations. With this simplifying approximation the observed decay rates and shift rates of the peak velocity are well accounted for. The reason is that from the centre to the peak of the vortex, the vortex is close to solid-body rotation and the linear Ekman pumping law is known to be approximately valid even in the nonlinear regime (Greenspan 1968). A direct comparison of the predicted evolution based on the linear pumping relation with the observations shows that the law is not valid beyond the peak of the vortex. The actual Ekman pumping is somewhat stronger in that region where the velocity decreases than the linear law predicts, and the steepening of the profiles in the numerical solutions is correspondingly less pronounced than in the laboratory observations.

2. Laboratory experiments

2.1. *Generation techniques*

The laboratory experiments were performed in a cylindrical Perspex tank placed on top of a rotating table (see figure 1). Velocity measurements were performed by means of streak photography of tracer particles floating on the free surface; for this purpose a remotely controlled photo camera was mounted in the rotating frame at some distance above the fluid surface. Velocities were calculated by measuring the lengths of the streaks on the photographs. Dye-producing crystals dropped in the tank provided qualitative information about the flow below the surface.

Cyclonic vortices were created by applying the so-called 'collapse technique', the basic set-up of which is shown in figure 1: the rotating tank is filled with a homogeneous fluid, and a bottomless cylinder with an internal diameter $2R_0$ is placed concentrically in the tank, with the fluid inside the inner cylinder at a level differing from that outside it. When the inner cylinder is withdrawn vertically, a gravity-driven flow arises in radial direction. This radial motion is deflected by the Coriolis force, and after a period of typically π/Ω an equilibrium state is reached in which the flow is close to purely azimuthal. When the difference in level ΔH is of the same order of magnitude as the average water depth, lifting of the cylinder ususally results in a vigorous turbulent flow in the centre of the tank. Although this flow is initially three-dimensional, after typically 2–3 rotation periods the fluid motion is observed to become nearly two-dimensional, taking the appearance of a horizontal swirl flow around the axis. Inertial waves are clearly involved in this process (see Greenspan 1968), but a firm theoretical basis explaining the two-dimensionalization of the

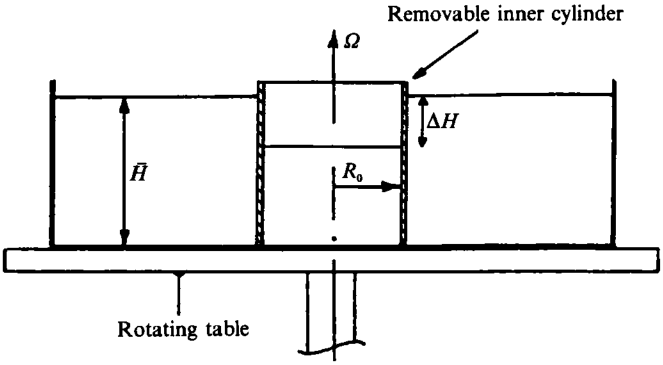

FIGURE 1. A schematic drawing of the laboratory set-up used for producing barotropic vortices. The diameter of the tank is 92.5 cm and it has a depth of 30 cm. The working depth $\bar{H}$ of the tank was varied between 5 cm and 25 cm (measured at rest). The Coriolis parameter $f = 2\Omega$ (in rad s^{-1}) was varied in the range 0.9 s^{-1} to 2.1 s^{-1} (Ω denotes the angular velocity of the turntable). Further details for various experiments are given in table 1.

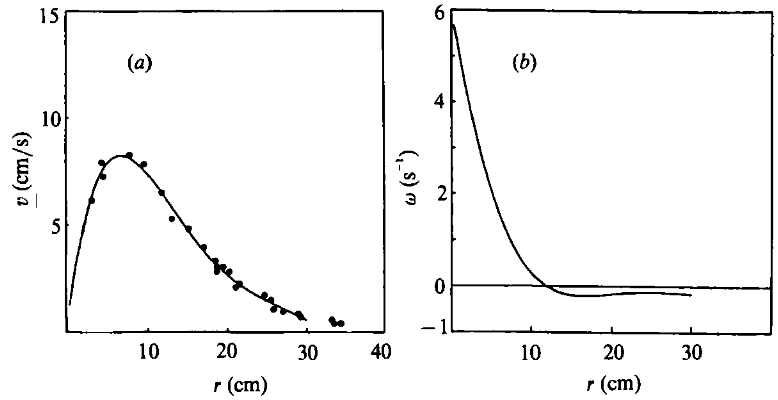

FIGURE 2. (*a*) The radial distribution of azimuthal velocity of a typical cyclonic, barotropic vortex. Measured velocities are indicated with black dots while the curve is a fourth-order polynomial. (*b*) The radial vorticity distribution, derived from the polynomial approximation of the velocity field.

vortices is to the best of our knowledge still lacking. For our purposes here, it suffices to note that whenever strong vertical motions occur, they are quickly subdued. As can be understood from conservation of angular momentum, cyclonic vortices are created by taking the fluid level inside the inner cylinder lower than outside.

Stable cyclonic vortices were also created by continuously withdrawing fluid from a sink located at the centre of the tank bottom. The radial motion induced by the sink is deflected in the cyclonic direction and when the sink forcing is stopped the flow is observed to become purely azimuthal within a few rotation periods.

Anticyclonic vortices are not discussed here because they are usually centrifugally unstable if the Rossby number is not small (see Kloosterziel & van Heijst 1991).

2.2. *Observed evolution of stable cyclones*

We determine the structure of a circular vortex by measuring the azimuthal velocity v as a function of the radius r, as measured from the vortex centre. A typical example of the velocity distribution of a laboratory cyclone is provided in figure 2(*a*). The experimental data are denoted by dots and the solid curve is a polynomial fit to the

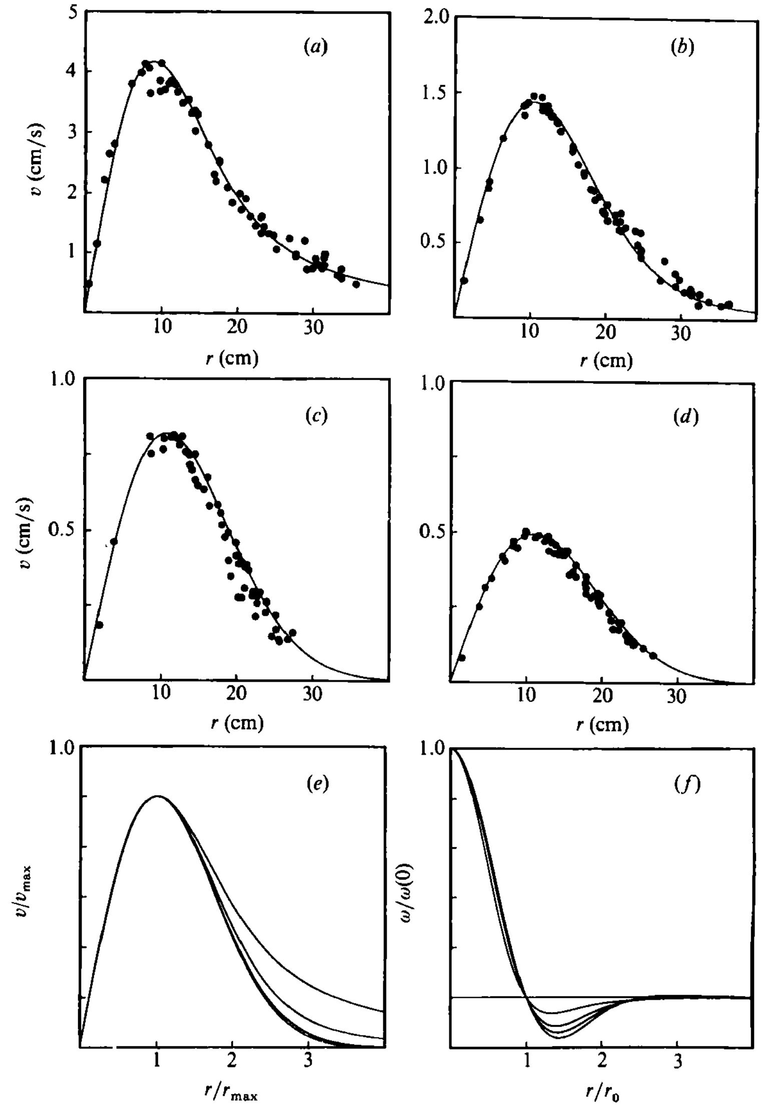

FIGURE 3. The radial distribution of the azimuthal velocity measured at the free surface of a cyclonic vortex created with the collapse technique at successive times after withdrawal of the cylinder: (a) $t = 19.2T$, (b) $38.4T$, (c) $48.0T$ and (d) $57.6T$, with $T = 6.25$ s the rotation period of the turntable. Experimental data are denoted by black dots while the curves are fitted to the data. The scaled curves (for an explanation, see text) are presented in (e). (f) The scaled vorticity profiles corresponding to the curves fitted through the data. Experimental parameters are: $\bar{H} = 13.8$ cm, $\Delta H = 10.9$ cm, $R_0 = 14.5$ cm, $\Omega = 1.0\,\mathrm{s}^{-1}$.

data. Information about the vorticity can be obtained by using the curve fitting the velocity data as a representation of $v(r)$; the vorticity distribution $\omega(r)$ is then calculated according to

$$\omega(r) = \frac{1}{r}\frac{\mathrm{d}\,rv(r)}{\mathrm{d}r}.$$

The vorticity profile associated with the azimuthal velocity distribution of figure 2(a) is shown in figure 2(b). Obviously, the cyclone has positive vorticity in its centre, while it is enclosed by an outer region of negative vorticity. According to figure 2(b), the vorticity takes a maximum value near the axis. In particular at smaller radii the vorticity profile is strongly dependent on the shape of the $v(r)$ profile, but because data are lacking in this centre region, the exact vorticity distribution near the origin is uncertain. Observational evidence indicates that for the laboratory vortices studied here the vorticity amplitude is always maximal close to the centre of the vortex.

For obtaining a reasonably accurate picture of the evolution of the form of the flow profiles, low-order polynomials are not a good choice for fitting the data with. In most cases the data can only be poorly fitted by such polynomials. The 'vorticity' derived by differentiation of the polynomial in such cases does not provide a reliable representation of the actual vorticity distribution in a vortex. Instead we used a family of curves that did a much better job. These curves are of the form

$$v(r) = UP(r/L)\exp\{-\tfrac{1}{2}(r/L)^2\},$$

with U an appropriate velocity amplitude, L a lengthscale and P a polynomial with $P(0) = 0$. The 'vorticity' corresponding to each of these polynomials is a polynomial solution of the Laguerre equation. It was found that at each instant the observed flow profiles could closely be approximated by a member of this family of curves.

In figure 3(*a–d*) the velocity distribution of a barotropic cyclonic eddy is fitted with one of these curves at four consecutive times. This vortex was produced with the collapse technique. The profiles are seen to be everywhere close to the measured velocities. The difference in form of the velocity distributions is elucidated by scaling the fitted curves onto each other. For this each profile is scaled with the maximum velocity $v_{\max}$ and the radial coordinate with the position of peak velocity $r_{\max}$. The scaled profiles thus all have a maximum at $R = r/r_{\max} = 1$ of $V(R = 1) = 1$. The result is shown in figure 3(*e*). It is seen that for increasing time the velocity profiles fall off faster to zero for $R > 1$. The increased steepness of the velocity profiles implies that the amplitude of the negative vorticity becomes larger relative to the amplitude of the core. This can be seen in figure 3(*f*) where the scaled vorticity profiles corresponding to the curves of figures 3(*a*)–3(*d*) are shown. Each profile has been scaled by its amplitude at $r = 0$ and the radial coordinate by the position r_0 at which the vorticity changes sign.

In figure 4 a similar sequence is shown but now for a sink vortex. There is somewhat more scatter in figures 4(*c*) and 4(*d*) but in each of figures 4(*a*)–4(*d*) the fits do appear to provide a reliable picture of the actual structure. Figure 4(*f*) therefore indicates that with increasing time the sink vortex also considerably steepens.

This means that the vortices are evolving towards a barotropically more *unstable* state (see Gent & McWilliams 1986; Flierl 1988; Carton & McWilliams 1989), and this can lead to dramatic changes in the character of the flow (see Kloosterziel & van Heijst 1991).

A main difference between the sink vortex and the collapse vortex is that sink vortices similar to that of figure 4 were never observed to become unstable whereas collapse vortices like that of figure 3 may become unstable. The reason for this is that the sink vortices start with a profile with hardly any negative vorticity around the core. In fact, the curve shown in figure 4(*a*) is very close to

$$v(r) \approx U/(r/L)\{1-\exp(-\tfrac{1}{2}(r/L)^2)\},$$

which for large r tends to potential flow. This is also clear from figure 4(*f*) where the corresponding scaled vorticity profile is seen to have almost no negative vorticity.

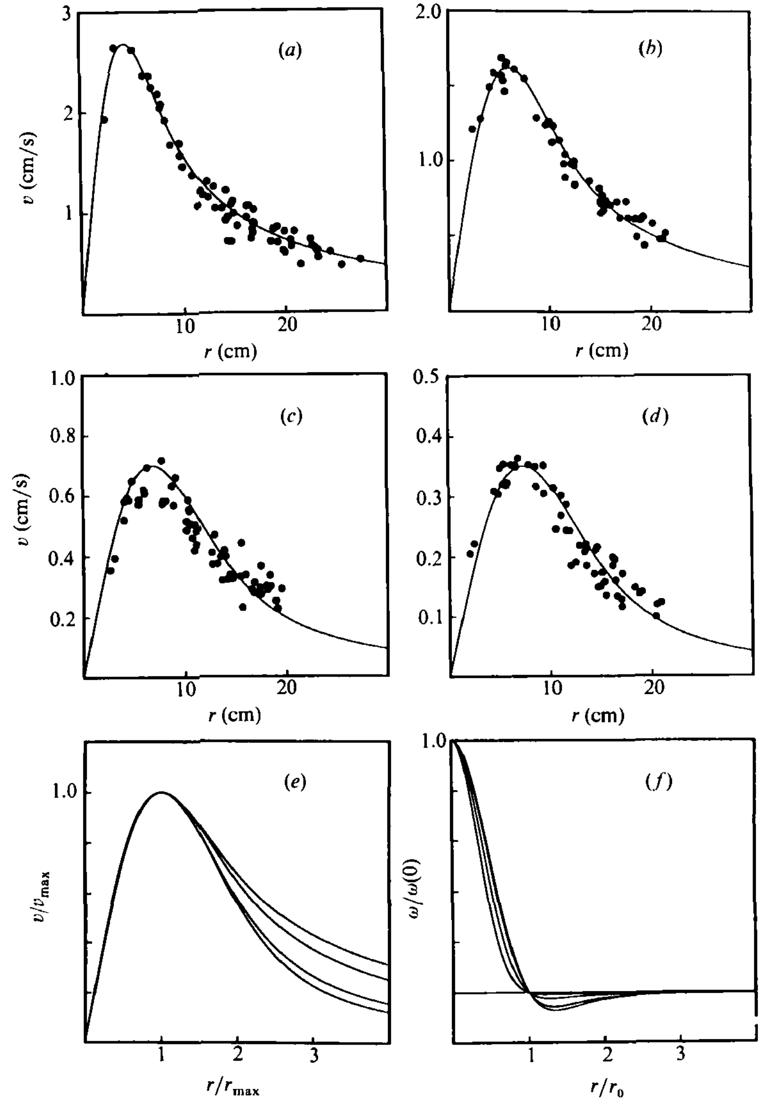

FIGURE 4. The azimuthal velocity distribution measured at the free surface of a sink-induced cyclonic barotropic vortex at successive times after the forcing was stopped: (*a*) $t = 8.9T$, (*b*) $14.4T$, (*c*) $27.6T$ and (*d*) $35.5T$, with $T = 8.4$ s the rotation period of the turntable. Experimental data are denoted by black dots while the curves are fitted to the data. The scaled curves (for an explanation, see text) are presented in (*e*). (*f*) The scaled vorticity profiles corresponding to the curves fitted through the data. Experimental parameters are: $\bar{H} = 12.4$ cm, $\Omega = 0.75\ \mathrm{s}^{-1}$.

The collapse vortex of figure 3 starts with a larger amplitude of negative vorticity (compare figures 3*f* and 4*f*). The curves shown in figures 3(*c*) and 3(*d*) are very close to

$$v(r) \approx U(r/L)\exp\{-\tfrac{1}{2}(r/L)^2\},$$

which is known to be a linearly unstable vortex. According to Gent & McWilliams (1986) and Carton & McWilliams (1989) this profile is unstable to wavenumber-2 perturbations if the flow is inviscid. The vortex of figure 3 did not show the growth of such an instability but similar vortices are sometimes (depending on the initial conditions) observed to transform into a tripole as a result of the growth of a

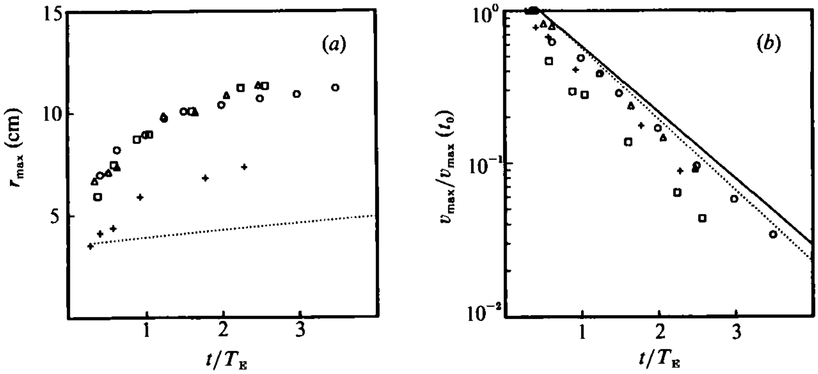

FIGURE 5. (*a*) The position of the peak velocity $r_{\max}$ and (*b*) peak velocity $v_{\max}$ as a function of the dimensionless time t^*. In each case the velocity amplitude in (*b*) has been scaled by the first of each observation series. Details about the four experiments are given in table 1. Four of the observed velocity distributions of experiment 3 (symbol ○) have previously been shown in figure 3 and four of the profiles of the sink vortex (experiment 4; symbol +) in figure 4. The dotted line in (*a*) indicates the shift of the peak velocity due to diffusion. The solid line in (*b*) indicates the exponential decay of linear Ekman dynamics whereas the dotted line indicates the correction for colder water (see text).

wavenumber-2 instability (see Kloosterziel & van Heijst 1991). Clearly the Ekman dissipation will damp the growth of the perturbation. So, the instability only manifests itself if the amplitude and the steepness are sufficiently high initially because otherwise the Ekman damping dissipates the flow before a critical steepness is reached and before a perturbation can grow to finite amplitude.

In analogy to what Greenspan & Howard (1963) pointed out for the spin-up of a fluid contained in a rotating cylinder with a rigid lid, the Ekman boundary layer is likely to play an essential role in the spin-down or spin-up of the vortices in the present experiments, much more than lateral frictional effects. In view of the well-known results concerning the linear Ekman dynamics (see Greenspan 1968; Pedlosky 1979) the appropriate timescale for the evolution of the vortices will be the Ekman time T_E. Based on the Ekman number $E = \nu/(\Omega H^2)$, the Ekman time is

$$T_E = H/(\nu\Omega)^{\frac{1}{2}}, \tag{1}$$

where H denotes the depth of the fluid layer at the tank centre when the fluid is in solid-body rotation (i.e. with no vortex present) and ν the kinematic viscosity of water. If one introduces the non-dimensional time $t^* = t/T_E$, and the spin-up or spin-down of the free-surface system is considered to consist of one-half of the problem of Greenspan & Howard, then the decay of the relative flow would be expressed as

$$v(r;t^*) = v_0(r)\,e^{-\gamma t^*}, \tag{2}$$

where $\gamma \approx 1$. This result, however, can only be expected to be valid for very small Rossby numbers.

That the decay of the laboratory vortices does not accord with (2) is clear from the observation that the functional form of the velocity distributions generally changes with increasing time (see figures 3 and 4), while the position of maximum velocity shifts outwards. The position of the peak velocity $r_{\max}$ as a function of the dimensionless time t^* for four different experiments is shown in figure 5(*a*). In figure 5(*b*) the maximum velocity $v_{\max}$ for these experiments is shown. The relevant details pertaining to these experiments are given in table 1. Figure 3 shows four profiles of

Exp. no.	Vortex type	Ω (s^{-1})	$\bar{H}$ (cm)	ΔH (cm)	T_E (s)	R_0 (cm)
1 □	collapse	0.94	19.8	17.0	187	14.5
2 △	collapse	0.75	13.8	10.3	146	14.5
3 ○	collapse	1.0	13.8	10.9	121	14.5
4 +	sink	0.75	12.4	—	131	—

TABLE 1. Experimental parameters for four laboratory experiments. $\bar{H}$ denotes the mean depth of the fluid layer, equal to the depth measured after an experiment when the table has been brought to a standstill and the fluid is motionless. With no vortex present the free-surface has the form $z(r) = H + (\Omega^2/2g)\,r^2$ and mass-conservation shows by integration that $\bar{H}$ is related to H according to $\bar{H} = H + (\Omega^2/4g)\,r_T^2$, where r_T is the tank radius.

experiment 3 whereas four profiles of experiment 4 are shown in figure 4. The Ekman time T_E, defined by (1), has been calculated for a kinematic viscosity $\nu = 1.14 \times 10^{-2}\ \mathrm{cm^2\,s^{-1}}$, a value appropriate for water at a temperature of 15 °C.

Linear Ekman dynamics predict pure exponential decay of the flow field and the position of peak vorticity would in that case be fixed. One might think that lateral diffusion accounts for the shifting peak. Typically diffusion leads to a shifting peak according to the formula

$$r_{\max}(t) = [2\nu t + r_{\max}^2(0)]^{\frac{1}{2}}$$

(see Kloosterziel 1990), and for comparison this is shown in figure 5(*a*) as a dotted line, starting with a value for experiment 4. It is seen that this shift rate is much smaller than the measured shift rate.

The velocity amplitude $v_{\max}$ (peak velocity) decreases close to exponentially, as can be inferred from figure 5(*b*), where $v_{\max}$ is plotted logarithmically versus t^*. The data shown here can be approximated very closely by straight lines with a slope of approximately $\gamma = 1.20$. The amplitude thus decays according to

$$v_{\max}(t^*) = v_{\max}(t_0^*)\exp\left[-\gamma(t^* - t_0^*)\right], \tag{3}$$

except for small t_0^* where deviations from this behaviour can occur. The Rossby number is not very small at these early stages, and strong nonlinear effects are important then. The deviation is especially clear for experiment 1; in figure 5(*b*) the amplitude decay is initially much faster for this experiment than for the other three experiments. The main difference is that the Rossby number for experiment 1 is at the earliest times approximately 3 whereas for the other ones it is close to 1.

The solid line in figure 5(*b*) denotes the pure exponential decay expected from linear Ekman dynamics. This line has a slope $\gamma = 1$. Diffusion leads to an acceleration of the decay rate but for vortices of this size it is a very small effect (see §3) and far too small to explain the faster decay rate.

It must be admitted here that the water temperature was not measured at the time the experiments were performed, and in some cases the actual water temperature may have been lower than 15 °C. For a temperature of 10 °C the kinematic viscosity is about $1.304 \times 10^{-2}\ \mathrm{cm^2\,s^{-1}}$ so the spin-down time may have been less than listed in table 1. The correction to the decay rate is indicated by a dotted line in figure 5(*b*). This line has a slope of $\gamma = 1.07$. It is seen that this cannot account for the faster decay rate of the laboratory vortices.

In the experiments no cover was used to reduce the air drag at the free surface, but this can also be shown to be of minor importance (see §3.2). The reason for the deviation from the linear Ekman damping will be discussed in §3: it is due to (weakly) nonlinear effects. Nevertheless, the timescale as given by (1), associated with the spin-down mechanism provided for by the bottom Ekman layer, is found to apply very well to the present problem.

3. Spin-down analysis

For circularly symmetric flows, away from the viscous boundary layers, the equations of motion are

$$\frac{\partial u}{\partial t}+u\frac{\partial u}{\partial r}+w\frac{\partial u}{\partial z}-\frac{v^2}{r}-2\Omega v=-\frac{1}{\rho}\frac{\partial P}{\partial r}+\nu\frac{\partial}{\partial r}\frac{1}{r}\frac{\partial ru}{\partial r}, \tag{4}$$

$$\frac{\partial v}{\partial t}+u\frac{\partial v}{\partial r}+w\frac{\partial v}{\partial z}+\frac{uv}{r}+2\Omega u=\nu\frac{\partial}{\partial r}\frac{1}{r}\frac{\partial rv}{\partial r}, \tag{5}$$

$$\frac{\partial w}{\partial t}+u\frac{\partial w}{\partial r}+w\frac{\partial w}{\partial z}=-\frac{1}{\rho}\frac{\partial P}{\partial z}+\nu\frac{1}{r}\frac{\partial}{\partial r}r\frac{\partial w}{\partial r}, \tag{6}$$

and the continuity equation is

$$\frac{1}{r}\frac{\partial ru}{\partial r}+\frac{\partial w}{\partial z}=0. \tag{7}$$

In order to facilitate the analysis, cylindrical coordinates (r,θ,z) have been introduced, with the vertical (z) axis coinciding with the axis of the tank, pointing upwards, and with the origin $r=0$ at the common axis of the vortex and the tank.

In (4)–(6) P stands for the reduced pressure, which for a rotating system is

$$P=p+\rho gz-\tfrac{1}{2}\rho\Omega^2r^2, \tag{8}$$

where p is the actual (thermodynamic) pressure in the fluid, and g the Earth's gravitational acceleration.

All motion is confined within the region

$$r\leqslant r_{\mathrm{T}},\quad 0\leqslant z\leqslant z_{\mathrm{free}}=H+\frac{\Omega^2}{2g}r^2+\eta,$$

where the free-surface elevation z_{free} has been written as a sum of the basic parabolic shape plus a deviation η. Here r_{T} denotes the tank radius (46.25 cm). The perturbation η from the parabolic shape is the 'dip' in the free surface that invariably accompanies the presence of a vortex, while H is the depth of the fluid at the centre of the rotating tank in the absence of any relative motion.

In barotropic flows like the ones studied here, vertical variations in the aximuthal velocity field are confined to a thin boundary layer at the bottom with an approximate thickness $\delta_{\mathrm{E}}\equiv(\nu/\Omega)^{\frac{1}{2}}$; under typical laboratory circumstances $\delta_{\mathrm{E}}\sim 1$ mm. The convergence of the horizontal flow in the bottom boundary-layer region induces a meridional circulation in the interior, that is, in the region outside the boundary layer. If the azimuthal flow has an amplitude U – the value of, say, the maximum velocity v_{max} – then the secondary motion in the interior typically has an amplitude of $O(E^{\frac{1}{2}}U)$. Typical values of the Ekman number for the laboratory experiments described here are $O(10^{-4})$. One well-established way of attacking the decay problem consists of seeking an expansion in the small parameters of the system. From the above it will be clear that the Ekman number certainly can serve as such, but other possibly small parameters can only be found by systematically scaling the equations, and this will be done below.

Without getting into the details here, it will be sufficient to indicate some of the steps (see Greenspan 1968 and Pedlosky 1979). The equations of motion and continuity are non-dimensionalized by using the following scales:

$$[u,v,w,P,\eta] = U\left[E^{\frac{1}{2}},1,E^{\frac{1}{2}},\rho\Omega L,\frac{2\Omega L}{g}\right],\quad [r,z,t] = [L,H,E^{-\frac{1}{2}}\Omega^{-1}].$$

Here U and L denote a typical velocity scale and a horizontal lengthscale, respectively. Hereafter all the dependent and independent variables are understood to be non-dimensional.

With these definitions, the non-dimensional expression for the free-surface shape becomes

$$h \equiv z_{\mathrm{free}}/H = 1+\tfrac{1}{2}Fr^2+2\epsilon F\eta. \tag{9}$$

In this expression two other characteristic parameters appear: the rotational Froude number F and the Rossby number ϵ, which are defined by

$$F = (\Omega L)^2/gH,\quad \epsilon = U/(\Omega L). \tag{10}$$

In conjunction with the equations of motion and the continuity equation, the boundary conditions for the vertical velocity have to be considered. At the free surface we have non-dimensionally

$$w(r,z=h) = \delta\left\{2F\frac{\partial\eta}{\partial t}+u\frac{\partial h}{\partial r}\right\}, \tag{11}$$

where $\delta = H/L$ is the aspect ratio. The dimensionless quantities u,v,w,P and η are expanded in powers of $E^{\frac{1}{2}}$ in the interior region. These power series are substituted in (4)–(7) and (11), and terms multiplied by the same power of $E^{\frac{1}{2}}$ are subsequently collected. To lowest order the pressure is hydrostatic and integration of the continuity equation then shows that

$$w(r,z) = w(r,z=0)-\delta\frac{1}{r}\frac{\partial ru}{\partial r}z. \tag{12}$$

By systematically collecting terms of the same order the following set of coupled equations is found which is correct to $O(E^{\frac{1}{2}})$:

$$\epsilon\frac{v^2}{r}+2v = 2\frac{\partial\eta}{\partial r}, \tag{13}$$

$$\frac{\partial v}{\partial t}+u(\epsilon\omega+2) = \frac{T_{\mathrm{E}}}{T_{\mathrm{d}}}\nabla^2 v, \tag{14}$$

$$2F\frac{\partial\eta}{\partial t}+\frac{1}{r}\frac{\partial}{\partial r}\{ruh\} = \frac{w(r,z=0)}{\delta}, \tag{15}$$

where ∇^2 is the horizontal Laplacian, T_{d} the timescale associated with horizontal diffusion of momentum, and ω the vorticity of the $O(1)$ interior flow:

$$\nabla^2 = \frac{\partial}{\partial r}\frac{1}{r}\frac{\partial}{\partial r}r,\quad T_{\mathrm{d}} = \frac{L^2}{\nu},\quad \omega = \frac{1}{r}\frac{\partial}{\partial r}(rv).$$

Equation (15) has been derived by using (12) for $z = h$ in conjunction with (11).

The set (13)–(15) has to be supplied with the bottom boundary condition for the

T_E	r_{max} (cm)	v_{max} (cm s^{-1})	F	T_E/T_d	ϵ
1.0	8.9	4.2	0.0067	0.017	0.45
1.99	10.4	1.4	0.0088	0.013	0.13
2.49	10.7	0.8	0.0097	0.012	0.071
2.98	10.9	0.5	0.010	0.012	0.044

TABLE 2. Typical values of some relevant parameters during various stages of decay of the cyclonic laboratory vortex shown in figure 3. Times are the same as in the caption of figure 3, but now measured in terms of the Ekman time.

vertical Ekman pumping, i.e. the right-hand side of (15) has to be specified. The boundary condition for w at $z = 0$ (at the 'top' of the bottom Ekman layer) is found by integrating the continuity equation for the boundary layer. This yields

$$w(r, z=0) = \tfrac{1}{2}\delta \frac{1}{r}\frac{\partial}{\partial r} rv \tag{16}$$

if the steady, *linear* boundary-layer equations are used to determine the $O(1)$ flow in the boundary layer. This identity states that the vertical Ekman pumping at the bottom is proportional to the vorticity of the interior motion.

Equation (16) is only valid for flows with vanishingly small Rossby numbers. No general law is known for arbitrary swirl flows with finite Rossby numbers. Often the steady Ekman flux calculations of Rogers & Lance (1960) are used. Their results are only valid for fluid in solid-body rotation over an infinite rotating disk. In the core of a typical vortex the fluid is close to solid-body rotation so one might apply their law locally. Beyond the position of peak velocity the fluid has decreasing circulation and there Rogers & Lance's Ekman pumping law cannot be applied. Instead of introducing some arbitrary assumptions we will therefore use (16) below for vortices with finite Rossby numbers. Comparison of the observations with the predictions based on (13)–(15) will show to what extent (16) is a good approximation. In what follows, our aim is to determine the evolution of v, and (14) has to be solved for this. The higher-order corrections for the azimuthal flow are not considered.

In (13)–(15) three parameters appear: the Rossby number ϵ, the rotational Froude number F and the ratio of Ekman time and diffusive time T_E/T_d. In table 2 typical values are given, which correspond to the four profiles shown in figure 3. The time is the elapsed time since the experiment was started and is given in units of the Ekman time, with $t = 1.0T_E$ corresponding to the profile shown in figure 3(*a*). For the lengthscale L the approximate position of peak velocity r_{max} was taken, and for the velocity scale U the peak velocity v_{max}. The ordering in magnitude is immediately apparent; at all times one has $F < T_E/T_d < \epsilon$. Both F and T_E/T_d are very small in this case, which is representative for most of the laboratory vortices studied here.

3.1. *Linear spin-down*

For arbitrary initial conditions and parameter values of ϵ, F and T_E/T_d the set (13)–(15) can only be solved numerically but before doing so we first investigate what the typical effect is of diffusion (non-zero parameter T_E/T_d), free-surface deformability (non-zero Froude number), and nonlinearities (non-zero Rossby numbers). We start here with the linear perturbations to linear Ekman decay. These effects will only be important in the final stages of decay when the Rossby number becomes as small as the Froude number and the diffusion parameter (see table 2).

We get the following set of equations when we put $\epsilon = 0$:

$$v = \frac{\partial \eta}{\partial r}, \tag{17}$$

$$2F\frac{\partial \eta}{\partial t} + \frac{1}{r}\frac{\partial}{\partial r}\{ru(1+\tfrac{1}{2}Fr^2)\} = \frac{1}{2}\frac{1}{r}\frac{\partial}{\partial r}rv, \tag{18}$$

$$\frac{\partial v}{\partial t} + 2u = \frac{T_{\mathrm{E}}}{T_{\mathrm{d}}}\nabla^2 v. \tag{19}$$

Free-surface effects will for the moment be neglected, and to lowest order (18) shows that $u = \frac{1}{2}v$. Substitution in (19) leads to the following equation for v:

$$\frac{\partial v}{\partial t} + v = \frac{T_{\mathrm{E}}}{T_{\mathrm{d}}}\nabla^2 v. \tag{20}$$

Putting $v'(r,t) = \mathrm{e}^t v(r,t)$, this reduces to the diffusion equation

$$\frac{\partial v'}{\partial t} = \frac{T_{\mathrm{E}}}{T_{\mathrm{d}}}\nabla^2 v'. \tag{21}$$

For vortices of small horizontal dimension relative to the size of the tank the results of Kloosterziel (1990) are applicable. A outward shift of peak velocity proportional to $t^{\frac{1}{2}}$ and a decay rate proportional to something between $t^{-\frac{1}{2}}$ and $t^{-\frac{3}{2}}$ are expected to be approximately valid. As a correction to linear Ekman decay, diffusion thus leads to an outward shift of peak velocity and an accelerated decay rate. In view of the smallness of the diffusion parameter both effects are under typical laboratory circumstances too small during most of the evolution (see table 2) to account for the observed discrepancy with the linear Ekman dynamics.

Next we investigate the combined effect of the free-surface deformability and the variation in fluid-layer depth and diffusion will for the moment be neglected. The general equation for the free-surface perturbation is obtained by substituting (17) and (19) in (18), while simultaneously putting $T_{\mathrm{d}} = \infty$:

$$\frac{\partial}{\partial t}\left\{4F\eta r - \frac{\partial}{\partial r}\left[(1+\tfrac{1}{2}Fr^2)\,r\frac{\partial \eta}{\partial r}\right]\right\} = \frac{\partial}{\partial r}r\frac{\partial \eta}{\partial r}. \tag{22}$$

This equation is also derived in Cederlöf (1988) where the effect of the free-surface deformability in the classical spin-up problem is studied.

For most initial conditions, solutions of (22) in closed form are hard to find. An exception is the exact solution to the classical spin-down problem presented in the Appendix, for which no expansion was needed. For the case of a vortex an expansion in F provides useful information. We put

$$\eta = \eta_0 + F\eta_1 + F^2\eta_2 + \dots, \quad v = \frac{\partial \eta}{\partial r} = v_0 + Fv_1 + F^2 v_2 + \dots, \tag{23}$$

and substitute this in (22). This leads to the following sequence of differential equations. At lowest order:

$$0 = \frac{\partial}{\partial t}\left\{\frac{\partial}{\partial r}r\frac{\partial \eta_0}{\partial r}\right\} + \frac{\partial}{\partial r}r\frac{\partial \eta_0}{\partial r}, \tag{24}$$

and at $O(F)$:

$$4r\frac{\partial \eta_0}{\partial t} = \frac{\partial}{\partial t}\left\{\frac{\partial}{\partial r}\tfrac{1}{2}r^3\frac{\partial \eta_0}{\partial r} + \frac{\partial}{\partial r}r\frac{\partial \eta_1}{\partial r}\right\} + \frac{\partial}{\partial r}r\frac{\partial \eta_1}{\partial r}. \tag{25}$$

The higher-order equations will not be of any concern here. From (24) we have

$$\eta_0(r,t) = \mathrm{e}^{-t}\zeta(r), \tag{26}$$

where $\zeta(r)$ gives the free-surface perturbation, to lowest order in both Rossby and Froude number, at $t = 0$. After substitution of this result in (25), multiplication by e^{+t} and integration over r and t, the following result is derived:

$$v_1(r,t) = t\,\mathrm{e}^{-t}\left\{\tfrac{1}{2}r^2\frac{\mathrm{d}\zeta}{\mathrm{d}r} - \frac{4M}{r}\right\}, \tag{27}$$

where $M(r)$ is the mass deficit, relative to the equilibrium distribution, due to the zero-order, free-surface perturbation at $t = 0$:

$$M(r) = \int_0^r \zeta(r)\,r\,\mathrm{d}r. \tag{28}$$

If $V(r)$ denotes $v(r, t = 0)$, the evolution is up to $O(F)$:

$$v(r,t;F) = \mathrm{e}^{-t}\left\{V(r) + tF\left[\tfrac{1}{2}V(r)r^2 - 4\frac{M(r)}{r}\right] + O(F^2)\right\}. \tag{29}$$

The mass-deficit term is always negative for cyclones, so the term within square brackets is positive everywhere for cyclonic vortices. This implies that the decay rate is *lessened* by the $O(F)$ effects as compared to the pure exponential decay of the linear Ekman dynamics.

The effect of a flexible free surface and an outward-increasing, basic layer depth can easily be understood as follows. Effectively the spin-down of the fluid is a consequence of the radial outward displacement of fluid particles by the interior Ekman circulation: angular momentum conservation shows that the decrease in azimuthal velocity of a particular fluid element is directly related to its net radial displacement. The free surface, however, can absorb part of the radial mass flux by simply raising itself, that is, the 'dip' in the free surface fills, and this effect is represented by the mass-deficit term in (29). A radially increasing equilibrium depth (the parabolic free surface) similarly decreases the magnitude of the radial displacement of fluid elements relative to the case of a layer of fluid of constant depth; this is represented by the first term within square brackets in (29).

The free-surface deformability and depth variations can induce a shift in the peak velocity, as the following example shows. Consider the vortex with the simple Gaussian shape that was seen to match well with the observations of the vortex of figure 3 in its final stages of decay (figures 3*c* and 3*d*). For such vortices the free-surface perturbation is (non-dimensionally)

$$\zeta(r) \propto c_0 - \mathrm{e}^{-\frac{1}{2}r^2} \tag{30}$$

where the constant c_0 has a value that makes $M(r_{\mathrm{T}}) = 0$. The tank radius is a little larger than four times the position of peak velocity for the vortex of figure 3(*c*, *d*). The position of the peak velocity corresponding to (30) is $r_{\max} = 1$, so for illustrating the consequences of (29), we take for the non-dimensional tank radius $r_{\mathrm{T}} = 4$. With (30)

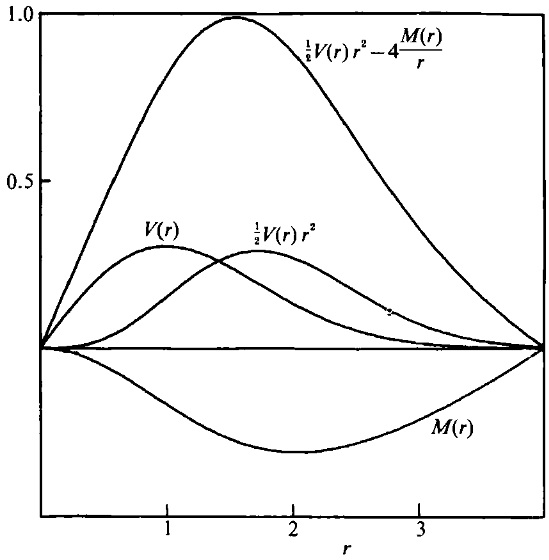

FIGURE 6. The terms that determine the first-order correction in (29), here for the case of the simple Gaussian vortex (see text).

given, the mass deficit M is easily calculated. The result is shown in figure 6, where the terms that determine the first-order correction in the evolution, according to (29), are shown together. Note that the vortex stretching due to the free-surface deformability is by far the larger of the two.

It is seen in figure 6 that the $O(F)$ term has a maximum at a radius larger than the position of peak velocity of the vortex at $t = 0$. As time increases, the position of peak velocity will thus shift outwards, while the amplitude simultaneously decays at a rate slower than with e^{-t}. This is also the case for characteristic other forms of the laboratory vortices. But, as is seen in table 2, the Froude number for the laboratory vortices is very small and the extra shift and slower amplitude decay due to free-surface effects will only play a role at very late times in the evolution.

3.2. *Nonlinear evolution*

In order to isolate the nonlinear effects we put the Froude number and the diffusion parameter equal to zero in (13)–(15) to obtain

$$\epsilon\frac{v^2}{r}+2v = 2\frac{\partial\eta}{\partial r}, \tag{31}$$

$$\frac{\partial v}{\partial t}+u(\epsilon\omega+2) = 0, \tag{32}$$

$$\frac{1}{r}\frac{\partial}{\partial r}ru = \frac{1}{2}\frac{1}{r}\frac{\partial}{\partial r}rv. \tag{33}$$

Equation (33) shows that the radial component of the Ekman circulation is $u = \frac{1}{2}v$, and by substitution in (32) we find

$$\frac{\partial v}{\partial t} = -\left(\tfrac{1}{2}\epsilon\omega+1\right)v. \tag{34}$$

This is a disguised form of *Wedemeyer's equation* (see Wedemeyer 1964; Venezian 1970). Wedemeyer's equation can easily be transformed into a damped wave equation by substitution of $v' = \frac{1}{2}\epsilon r v$ and introduction of the variable $s = \frac{1}{2}r^2$. This can further be solved for a given initial velocity distribution with the method of characteristics. Let us merely indicate here what the behaviour of solutions of this equation will be.

Equation (34) tells us a few things. First of all, it may be noted that in the core of a cyclone, where ω is positive, the rate of decay will generally be larger than in the linear case ($\epsilon = 0$). In this region the advection of vorticity by the radial component of the Ekman circulation, u, increases the decay rate. At larger radii, the rate of decay is smaller than in the linear case since the vorticity will generally be negative there, except for potential flow. It is thus anticipated that this combination of effects leads to the steepening of a velocity profile. It may be remembered here that the phrase steeper flow profile is used here to mean one for which the velocity falls off to zero faster for increasing $r > r_{\max}$.

For small-enough Rossby numbers, an expansion can be used to further investigate the behaviour of solutions of (34). For that purpose we write

$$v = v_0 + \epsilon v_1 + \ldots, \quad \omega = \omega_0 + \epsilon\omega_1 + \ldots, \tag{35}$$

and substitute this in (34). Collecting terms of the same order in ϵ, the following sequence of equations is obtained. At lowest order

$$\frac{\partial v_0}{\partial t} + v_0 = 0, \tag{36}$$

and at $O(\epsilon)$

$$\frac{\partial v_1}{\partial t} + v_1 = -\tfrac{1}{2}\omega_0 v_0. \tag{37}$$

Putting

$$v_0(r, t = 0) = V(r), \quad \omega_0(r, t = 0) = \frac{1}{r}\frac{\mathrm{d}}{\mathrm{d}r}(rV) = \tilde{\omega}, \tag{38}$$

and demanding that at $t = 0$, $v_1 = 0$, the solutions of the above equations are

$$v_0(r, t) = \mathrm{e}^{-t}V(r), \quad v_1(r, t) = (\mathrm{e}^{-2t} - \mathrm{e}^{-t})\,\tfrac{1}{2}\tilde{\omega}(r)\,V(r),$$

and so on for higher-order terms. The solution of (34) can therefore be written as the series

$$v(r, t; \epsilon) = \mathrm{e}^{-t}V(r)\,\{1 + \epsilon(\mathrm{e}^{-t} - 1)\,\tfrac{1}{2}\tilde{\omega} + O(\epsilon^2)\}. \tag{39}$$

For small ϵ the lowest-order correction will dominate over the higher-order terms. To illustrate the consequences of the lowest-order correction, the function

$$f(r; a) = V(r)\,(1 - a\tilde{\omega}), \quad V(r) = \tfrac{1}{2}r\,\mathrm{e}^{-\frac{1}{2}r^2} \tag{40}$$

is plotted in figure 7. The parameter a is interpreted as

$$a = \tfrac{1}{2}\epsilon(1 - \mathrm{e}^{-t}),$$

and an increasing value of a thus corresponds – for fixed ϵ – to increasing time. In figure 7 the result is shown for $a = 0, 0.2$ and 0.5. The curve with $a = 0$ corresponds to the curve that was fitted to the data in figure 3(*c*). The curves shown in figure 7 thus give an indication of the evolution of a typical vortex to lowest order in Rossby number. It is clear that the nonlinearity induces a shift in the position of peak

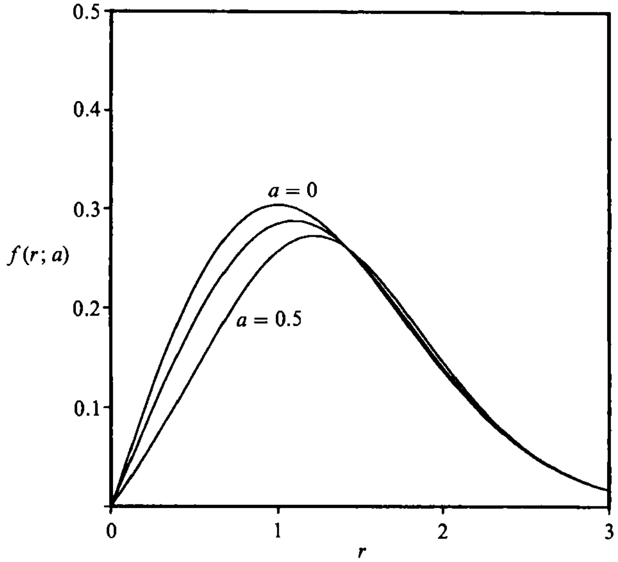

FIGURE 7. The function $f(R; a)$, defined by (40), for three different values of the parameter a.

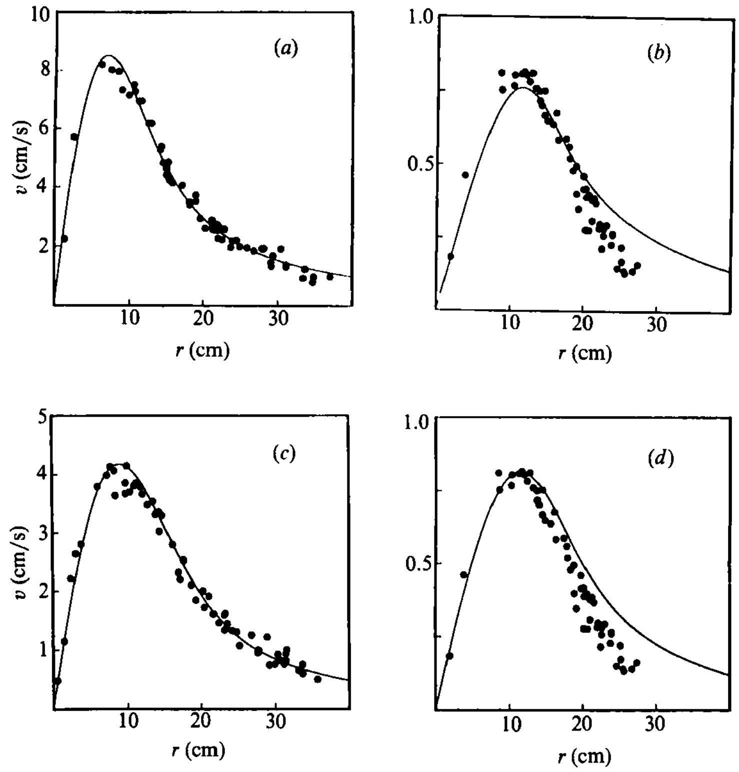

FIGURE 8. (a) The initial condition (solid line) for the numerical integration of (13)–(15) and (b) the result of the integration. The black dots denote the observed velocity distribution from experiment 3. Times are (a) $t = 0.41T_E$ after starting the experiment and (b) $t = 2.49T_E$. The relevant parameter values at the start of the integration were $\epsilon = 1.16$, $T_E/T_d = 0.028$, $F = 0.0042$. (c) The initial condition for the integration starting at a later time. Relevant parameters are given in the top row of table 2. (d) The result is like (b), compared with the observation at time $t = 2.49T_E$.

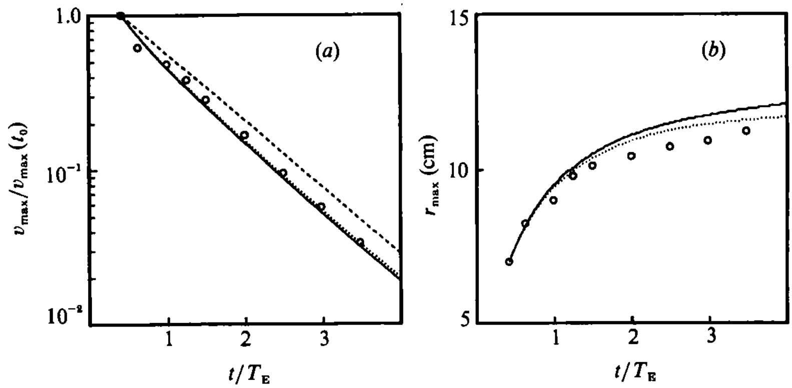

FIGURE 9. Graphs comparing the (*a*) amplitude decay and (*b*) shift of peak velocity of the numerical integration of (13)–(15) with the observations of experiment 3. The initial condition is shown in figure 8(*a*). In (*a*) and (*b*) the solid line denotes the decay with all effects included, and the dotted line the nonlinear evolution without free-surface effects or diffusion. The dashed line in (*a*) denotes the linear Ekman decay.

velocity and a *form* change. In fact, since the curves almost coincide over most of the range $r > r_{\text{max}}$, a rescaling of these curves would show a distinctive steepening of the profile, which is in accordance with the laboratory observations. Moreover, the rate of decay is speeded up by the nonlinearity, and is faster than with e^{-t}. For high Rossby numbers the steepening and faster decay are more pronounced than for small Rossby numbers.

The complete set (13)–(15) has numerically been solved while using the Ekman pumping relation (16). The evolution of v has been determined by solving (14) with a Crank–Nicholson scheme for the diffusive part and an upwind differencing scheme for the advective part. In order to determine the radial component of the Ekman circulation u, a second-order ordinary differential equation for u was obtained by elimination between (14) and (15) and using (13). This equation was solved with a shooting method with the boundary condition $u = 0$ at $r = 0$. At the tank wall one finds by integration of (15) that u should satisfy (see the Appendix) $u(r_{\mathrm{T}}, t) = \frac{1}{2}v(r_{\mathrm{T}}, t)/(1+\frac{1}{2}Fr_{\mathrm{T}}^2)$.

To illustrate the results the vortex of figure 3 is considered (experiment 3; see tables 1 and 2). As initial condition for (13)–(15) the fit through the data at the earliest time was chosen. This initial condition is shown in figure 8(*a*). The values of the relevant parameters at the start of the numerical integration of the equations are given in the caption. In figure 9(*a*) the amplitude decay of the numerical solution is compared with the observed decay of this vortex. The solid line denotes the result with all effects retained, i.e. with non-zero ϵ, F and diffusion. The dotted line represents the result of an integration for which only the nonlinearities were retained, that is, with no diffusion and no free-surface effects. As was to be expected from the magnitudes of the Froude number and the diffusion parameter, the difference is very small. The dashed line gives the pure linear Ekman decay, with no diffusion, free-surface effects or nonlinearities. It is seen that the numerical integration closely matches the observations and gives the correct slope. The decay rate at the very early times is a little too high so that at later times the simulation amplitude is systematically slightly lower than the observed amplitude. Since the solid line and the dotted line are very close it can be concluded that the accelerated decay rate is due to the advection of relative vorticity, i.e. it is a nonlinear effect. Closer inspection shows that the slope of the full simulation is essentially constant after the fifth data point for which the Rossby number is about 0.23. Before that the curve is slightly convex, and the rate of decay is thus not simply exponential.

In figure 9(*b*) the peak velocity position according to the numerical integration is compared with the observed position. The solid line again denotes the case with all effects incorporated whereas the dotted line corresponds to the case of no diffusion and no free-surface effects. As expected the shift rate is slightly faster if diffusion and free-surface effects are incorporated. In both cases there is a slight overshooting in the numerical solution as compared to the observations. The curves are however easily within the error of the positions of peak velocity (we estimate an error of at least 1 cm in certain cases).

In figure 8(*b*) the profile of the numerical integration at time $t = 2.49T_E$ is shown together with the observed velocity distribution. We note that the position of peak velocity is indicated well by the numerical solution (solid line), but the amplitude is a little too low. In figure 3(*c*) the same distribution is shown with the fit from which the observed seventh data points in figures 9(*a*) and 9(*b*) were determined. There is a major difference between the observed velocity distribution and the numerical solution beyond the peak. The velocity profile has become much steeper in the laboratory than the solution of the set (13)–(15). Three possible causes can be discerned. First of all we took the linear Ekman pumping law (16) for the boundary condition at the bottom. Secondly, air drag at the free surface has been neglected and thirdly surface tension has been assumed to be negligible. The non-dimensional parameter associated with surface-tension effects is an order of magnitude smaller than the Froude number in these experiments (it is the ratio of the capillary lengthscale and the typical lengthscale of the vortex), and this effect is therefore entirely negligible. Air drag (no cover over the tank was used in these experiments) leads to Ekman pumping at the free surface. A linear boundary-layer analysis, neglecting the curvature of the free surface, yields that the pumping at the free surface is (nondimensionally)

$$w_{\text{top}} = -\frac{1}{2}\frac{\Delta}{1+\Delta}(\epsilon\omega+2),$$

with

$$\Delta = \frac{\mu_A}{\mu_W}\left(\frac{\nu_W}{\nu_A}\right)^{\frac{1}{2}},$$

where the subscripts refer to water and air and μ is the molecular viscosity and ν the kinematic viscosity. For typical water and air temperatures we have $\Delta \approx 4.4\times 10^{-3}$.

The extra Ekman pumping increases the secondary radial motion. The correction to u due to the surface pumping is an increasing function of radius. This leads to an increased steepening but this effect again turned out (numerically) to be far too small to account for the discrepancy between the numerical solution and the observations.

Also, it can easily be shown that the sidewall is not likely to play any role in an explanation for the discrepancy. A simple order of magnitude estimate based on the diffusion equation shows that for the influence of the sidewall to penetrate just a few centimeters into the interior much more time is needed than the actual lifetime of the vortices.

By systematically performing the integration at later times, it was found that the discrepancy in steepness remains not only for Rossby numbers of $O(1)$ but also for Rossby numbers of an order of magnitude smaller. We performed the integration starting at a later time than the case of figure 8(*a*). In figure 8(*c*) we show the initial condition which is of experiment 3 at time $t = 1.0T_E$. This corresponds to the third data point in figure 9. At this time (see table 2) the Rossby number has fallen to a value of $\epsilon = 0.45$. We integrated the evolution equations with the linear Ekman pumping law to the same time as that of figure 8(*b*) (the seventh data point in figure 9). The result is shown in figure 8(*d*). Having started with a smaller Rossby number, the peak amplitude is much better approximated by the numerical solution but the discrepancy in steepness remains. The amplitude decay of the numerical solutions starting at this later time runs exactly parallel to the solid curve in figure 9(*a*), and is everywhere very close to the observed amplitudes. It appears therefore that for moderate Rossby numbers (< 0.5, say) the linear Ekman pumping law is valid in the core of the vortex.

However, we have to conclude that (16) is a bad approximation to the actual Ekman pumping rate for radii around and beyond the position of peak velocity. The actual Ekman pumping rate in the region of decreasing circulation is apparently higher than what is predicted by a linear boundary-layer analysis if the Rossby number is not negligibly small. In fact, beyond the peak where the relative vorticity is negative according to (16) there is Ekman suction into the boundary layer and we should therefore say that in that region the Ekman suction is not as strong as linear analysis predicts.

Instead of using the linear law (16) we have also used the numerically determined Ekman pumping law of Rogers & Lance (1960). This only concerns solid-body rotation over an infinite plate but many authors have applied the result to other flow types (see Weidman 1976). Weidman gives an accurate approximation which in dimensionless form corresponds to an Ekman pumping law of the following form:

$$w(r, z=0) = \delta\Gamma(r)\frac{K[1+\epsilon\Gamma(r)]^{\frac{1}{2}}}{1+b+\epsilon\Gamma(r)},$$

with $K = 1.36961$, $b = 0.353$. $\Gamma = v/r$ is the angular velocity of the flow relative to the bottom plane. This is correct for all Rossby numbers but only for a constant positive angular velocity, i.e. for (cyclonic) solid-body rotation. In order to investigate whether this law might be applicable to flows with variable angular velocity, we have used this law for the boundary condition at the bottom instead of (16). It clearly implies Ekman pumping instead of suction in the region beyond the peak and it will therefore lead to a faster steepening of the flow profiles. Integration of (13)–(15) showed that the steepening rate and amplitude decay with this law are far too high. The appropriate Ekman pumping law for vortices with finite Rossby numbers remains therefore an open question.

4. Discussion

The observations discussed in §2 show that the evolution of a typical stable laboratory cyclone is characterized by a distinctive steepening of the velocity profiles. The result of this is that the vorticity distribution changes to a form that is barotropically more unstable. The analysis presented in §3 shows that these changes are brought about by the presence of the interior Ekman circulation which results in the advection of relative vorticity. This is a nonlinear effect which also increases the decay rate (as compared to linear Ekman decay). For large-enough Froude numbers the effects of the advection of relative vorticity can be counteracted by the free-surface deformability. In fact, if one neglects diffusion, and expands all variables in

		Form change†	
	Decay rate	Widening/steepening	Shift of $v_{\max}$
Free surface	$< e^{-t}$	widening	outward
Advection of vorticity	$> e^{-t}$	steepening	outward
Lateral diffusion	$> e^{-t}$	see caption	outward

† For cyclones only

TABLE 3. A list of the effects of the mechanisms in the left-hand column on the evolution of a typical laboratory vortex. The decay rate is measured relative to the case of linear Ekman decay. Regarding diffusion, in Kloosterziel (1990) it is shown that if an initial vorticity distribution $\omega^0(r)$ is square-integrable according to

$$\int_0^\infty |\omega^0(r)|^2 \exp(+\tfrac{1}{2}r^2)\, r\,\mathrm{d}r < \infty,$$

and if for some integer $n \geqslant 0$

$$\int_0^\infty \omega^0(r)\, r\,\mathrm{d}r = 0, \ldots, \quad \int_0^\infty \omega^0(r)\, r^{2n-1}\,\mathrm{d}r = 0, \quad \int_0^\infty \omega^0(r)\, r^{2n+1}\,\mathrm{d}r \neq 0,$$

then, if the vorticity evolves according to the diffusion equation, for large time the similarity solution

$$\omega(r,t) = \frac{c}{b(t)^{2n+2}} L_n(\tfrac{1}{2}r^2/b(t)^2) \exp(-\tfrac{1}{2}r^2/b(t)^2)$$

becomes dominant. Here c is a constant, $b(t) = (2\nu t + L^2)^{\frac{1}{2}}$, L_n a Laguerre polynomial of order n, t the time and L some lengthscale. So, all vortices that satisfy this criterion for the same n will asymptotically tend to the same form. Their initial forms may be quite different though, and it is therefore well possible that certain profiles when scaled during their diffusive evolution become wider instead of steeper. These results can also be applied to tank vortices if their horizontal scale is small compared to the size of the tank.

Froude number and Rossby number, then to first order in these parameters the evolution is given by

$$v(r,t;F,\epsilon) = \mathrm{e}^{-t}\left\{V(r) + \epsilon(\mathrm{e}^{-t}-1)\,\tfrac{1}{2}V(r)\frac{1}{r}\frac{\mathrm{d}}{\mathrm{d}r}(V(r)\,r) + tF\left[\tfrac{1}{2}V(r)\,r^2 - 4\frac{M(r)}{r}\right] + \ldots\right\}. \tag{41}$$

This is a mere linear combination of the results separately derived in §§3.1 and 3.2. The first term within curly brackets gives the uniform spin-down of the vortex. The presence of the second term induces an acceleration of the decay rate and steepening of the profile, but the third term decelerates the decay and opposes the steepening of the flow profile of a cyclone. Depending on the relative magnitude of the parameters F and ϵ, one of the two may dominate over the other. The effects of the three mechanisms – diffusion, free-surface deformability and advection of relative vorticity – are summarized in table 3.

Usually, for practical reasons the evolution of the laboratory vortices could not be monitored for Rossby numbers smaller than the Froude number. The steepening effect was therefore dominantly present in the observations of the evolving laboratory vortices.

By comparing the numerical solutions of (13)–(15) with the observations we inferred that the linear Ekman pumping law is not valid in the region of decreasing velocity of the cyclones. The actual Ekman suction in that region is weaker (or the Ekman pumping stronger) because the faster steepening has to be due to a larger radial component of the interior Ekman circulation. Rogers & Lance's (1960) Ekman pumping law for nonlinear spin-down has furthermore been contrasted with the observations. We find that it cannot be applied to the laboratory cyclones with finite Rossby numbers.

By using (14) one can in principle determine the interior radial component of the Ekman circulation. Neglecting diffusion one has

$$u(r;t) = \frac{-\partial v(r;t)/\partial t}{\epsilon\omega(r;t)+2},$$

and with (15) one gets (neglecting free-surface effects)

$$w(r,z=0;t) = \delta\frac{1}{r}\frac{\partial}{\partial r}ru(r;t).$$

By measuring the rate of change of the azimuthal velocity and the vorticity, the vertical Ekman pumping can thus be determined. However, precision measurements are needed for this programme which are far beyond the precision allowed by the streakline photography technique that has been used by us. This has to be left therefore for future work.

A number of the experiments described in this paper were carried out on a direct-drive turntable that was built more or less as a duplicate of a rotating table in use at the Department of Applied Mathematics and Theoretical Physics, University of Cambridge, UK. We are very grateful to Dr Paul F. Linden for his courtesy and his kind willingness to provide us with the required technical instructions and specifications. The authors also thank Dr Leo Maas for a number of stimulating discussions on the spin-down process. R.C.K. gratefully acknowledges financial support from the working group on Meteorology and Physical Oceanography (MFO) of the Netherlands Organization of Scientific Research (NWO) and financial support by ONR/DARPA under the University Research Initiative Program no. N0014-86-K-0758.

Appendix

An exact solution of (22), for arbitrary F, solves the classical spin-up problem. This solution is found by tentatively putting $\eta(r,t) = e^{-\gamma t}\mathscr{H}(r)$, with $\mathscr{H}$ an arbitrary function. If this is substituted in (22) and the new variable

$$y = \frac{1}{2}\frac{\gamma F}{1-\gamma}r^2 \tag{A 1}$$

is introduced, one finds

$$y(1-y)\frac{d^2\mathscr{H}}{d^2y}+(1-2y)\frac{d\mathscr{H}}{dy}+2\mathscr{H} = 0, \tag{A 2}$$

which is a standard hypergeometric differential equation (see Abramowitz and Stegun 1965). In this particular case the solution that is not singular at $y = 0$ is

$$\mathscr{H}(y) = \mathscr{F}(2,-1;1;y) = 2y-1 \tag{A 3}$$

($\mathscr{F}$ is a hypergeometric function). The value of γ is determined by the following consideration of (18). The term on the right-hand side of (18) is the local vertical mass flux pumped into the interior at the bottom due to the convergence of the boundary-layer flow. On the left-hand side one first has the vortex stretching term that gives the rate of change of the local thickness of the free-surface perturbation, while the second term equals the divergence of the net radial mass flux in the interior. Multiplying (18) by r, and integrating from the tank centre (with which the vortex centre is assumed to coincide) to the tank wall, which is taken at the non-dimensional position $r = r_{\mathrm{T}}$, one obtains

$$2F\frac{\partial}{\partial t}M(r_{\mathrm{T}},t)+ur_{\mathrm{T}}(1+\tfrac{1}{2}Fr_{\mathrm{T}}^2) = \tfrac{1}{2}vr_{\mathrm{T}}, \tag{A 4}$$

where
$$M(r,t) \equiv \int_0^r \eta(s,t)\,s\,\mathrm{d}s \tag{A 5}$$

is proportional to the integrated mass deficit, relative to the equilibrium mass distribution. Mass conservation implies

$$\frac{\partial M(r_{\mathrm{T}},t)}{\partial t} = 0$$

since the Ekman circulation merely redistributes mass (in fact, one has, by definition, $M(r_{\mathrm{T}},t) = 0$). One is therefore left with the identity

$$u(r_{\mathrm{T}},t)\,(1+\tfrac{1}{2}Fr_{\mathrm{T}}^2) = \tfrac{1}{2}v(r_{\mathrm{T}},t).$$

The left-hand side here gives the mass flux into the passive sidewall layer (which has a sandwich structure consisting of a $E^{\frac{1}{3}}$-layer within a $E^{\frac{1}{4}}$-layer) needed for returning the radial mass flux, via the bottom Ekman layer, into the interior (see Greenspan 1968). Vertical integration of the $O(1)$ radial flux in the bottom boundary layer shows that it is equal to $\frac{1}{2}v$. If one uses (19) in the above identity, neglecting diffusion, it follows that the azimuthal flow decays at the tank wall (outside the sidewall boundary layer) according to

$$v(r_{\mathrm{T}},t) = v(r_{\mathrm{T}},0)\exp\left(\frac{-t}{1+\frac{1}{2}Fr_{\mathrm{T}}^2}\right). \tag{A 6}$$

This shows that necessarily

$$\gamma = \frac{1}{1+\frac{1}{2}Fr_{\mathrm{T}}^2}, \tag{A 7}$$

and if this is substituted in (A 3) with y as given by (A 1), it is found that

$$\eta(r,t) = \mathrm{e}^{-\gamma t}\left\{2\left(\frac{r}{r_{\mathrm{T}}}\right)^2-1\right\}. \tag{A 8}$$

For all t one has (mass conservation)

$$\int_0^{r_{\mathrm{T}}} \eta r\,\mathrm{d}r = 0.$$

It is readily seen that this particular solution corresponds to the case in which at $t = 0$ the fluid in the rotating tank is in solid-body rotation relative to the rotating reference frame. It solves therefore the classical *linear* spin-down problem discussed by, for example, Greenspan & Howard (1963). In that paper the problem of solving (22) for the spin-up or spin-down problem was attacked by seeking an expansion in Froude number. At both zero order and first order in the Froude number, the fluid was found to spin up as a solid body. The results derived here show that in fact no expansion in Froude number is necessary and that at all orders the fluid spins up in the same way.

REFERENCES

ABRAMOWITZ, M. & STEGUN, I. A. 1965 Handbook of Mathematical Functions. Dover.

CARNEVALE, G. F., KLOOSTERZIEL, R. C. & HEIJST, G. J. F. VAN 1991 Propagation of barotropic vortices over topography in a rotating tank. *J. Fluid Mech.* **233**, 119–139.

CARTON, X. J. & MCWILLIAMS, J. C. 1989 Barotropic and baroclinic instabilities of axisymmetric vortices in a quasi-geostrophic model. In *Mesoscale/Synoptic Coherent Structures in Geophysical Turbulence* (ed. J. C. J. Nihoul & B. M. Jamart), pp. 225–244. Elsevier.

CEDERLÖF, U. 1988 Free-surface effects on spin-up. *J. Fluid Mech.* **187**, 395–407.

FLIERL, G. R. 1988 On the instability of geostrophic vortices. *J. Fluid Mech.* **197**, 349–388.

GENT, P. R. & MCWILLIAMS, J. C. 1986 The instability of circular vortices. *Geophys. Astrophys. Fluid Dyn.* **35**, 209–233.

GREENSPAN, H. P. 1968 *The Theory of Rotating Fluids.* Cambridge University Press.

GREENSPAN, H. P. & HOWARD, L. N. 1963 On a time-dependent motion of a rotating fluid. *J. Fluid Mech.* **17**, 385–404.

KLOOSTERZIEL, R. C. 1990 On the large-time asymptotics of the diffusion equation on infinite domains. *J. Engng Maths* **24**, 213–236.

KLOOSTERZIEL, R. C. & HEIJST, G. J. F. VAN 1991 An experimental study of unstable barotropic vortices in a rotating fluid. *J. Fluid Mech.* **223**, 1–24.

PEDLOSKY, J. 1979 *Geophysical Fluid Dynamics.* Springer.

ROGERS, M. H. & LANCE, G. N. 1960 The rotationally symmetric flow of a viscous fluid in the presence of an infinite rotating disk. *J. Fluid Mech.* **7**, 617–631.

SAUNDERS, P. M. 1973 The instability of a baroclinic vortex. *J. Phys. Oceanogr.* **3**, 61–65.

VENEZIAN, G. 1970 Non-linear spin-up. *Topics in Ocean Engineering*, vol. 2, pp. 87–96. Gulf.

WEDEMEYER, E. H. 1964 The unsteady flow within a spinning cylinder. *J. Fluid Mech.* **20**, 383–399.

WEIDMAN, P. D. 1976 On the spin-up and spin-down of a rotating fluid. Part 1. Extending the Wedemeyer model. *J. Fluid Mech.* **77**, 685–708.